

Fully Vacuum-Processed Perovskite Solar Cells on Pyramidal Microtextures

Lidón Gil-Escrig, Marcel Roß, Johannes Sutter, Amran Al-Ashouri, Christiane Becker, and Steve Albrecht*

Solar cells based on metal halide perovskites have attracted tremendous attention due to the rapid increase in performance of single junctions and tandem solar cells. Recently, highest perovskite/silicon tandem efficiencies are realized with front-side polished silicon wafers or adapted microstructure of textured silicon solar cells. One way to integrate perovskite top cells on typical micrometer-sized pyramidal structures, is conformal vacuum-based perovskite deposition. Herein, fully vacuum-based perovskite solar cells are developed on top of random pyramidal microtextured glass substrates with a pyramid size up to 9 μm . This method allows improvement of the light management of the textured perovskite solar cell and resembles the typical pyramid topography of silicon solar cells as a step toward monolithic tandem integration. Moreover, to improve the quality of the perovskite on the textured substrates, three different methylammonium lead iodide (MAPbI_3) films are tested by adjusting the rate ratio of the precursors. Optimized ratios for textured substrates with higher PbI_2 rates enable a transient photoluminescence decay time above 0.75 μs approaching that of planar substrates at around 1.2 μs . Finally, a efficiency over 15% is achieved, which is, to the best of our knowledge, the first reported device on microscopically textured glass by co-evaporated ion.

industrial and scientific aspects in the last decade due to their exceptional optoelectronic properties. These are, e.g., a high absorption coefficient, long minority charge carrier lifetime, long diffusion length as compared with the typical absorber thickness, and easy-to-tune bandgap by halide and cation exchange.^[1–3] The power conversion efficiency (PCE) of the perovskite solar cells has experienced a rapid growth, with a certified PCE of 25.2% which is approaching the efficiencies of best crystalline silicon (c-Si) single junction solar cells.^[4] In addition, recent perovskite/silicon tandem efficiencies overcome best c-Si single junction solar cells significantly.^[5]

When correlating and comparing the different fundamental losses of lead halide perovskite solar cells with other solar cell technologies, the V_{oc} and fill factor (FF) losses should be improved further to get closer to theoretical efficiency limits.^[6]

However, also the short-circuit current

density (J_{sc}) and with that the optical losses of lead halide perovskite solar cells are behind silicon and GaAs champion cells.^[6] Therefore, not only the electrical properties need to be improved but also the light management within single junctions or perovskite top cells that are integrated in full perovskite/silicon tandem solar cell device stacks. Trapping more light in the active layers and particularly reducing the optical losses from reflection and parasitic absorption is therefore highly important.

So far, most perovskite deposition methods rely on solution-based spin coating^[7] or blade coating,^[8,9] leading to the highest reported efficiencies in both perovskite single junction^[4] and tandem solar cells.^[5] Solution processing of perovskite layers favors planar substrates. Therefore, there exist many reports on light management concepts utilizing planar interfaces of the perovskite: light management in perovskite single junction and tandem solar cells can be provided by antireflective films, such as low refractive index NaF or MgF_2 on the glass substrates.^[10,11] Proper light management can also be realized by adjusting the thickness and refractive indexes of the different layers in a standard perovskite solar cell^[12] or the use of a properly designed interlayer in a tandem device.^[13] Another approach compatible with planar perovskite layers is the attachment of textured antireflective foils,^[14] textured polydimethylsiloxane (PDMS),^[15] or textured polyethylene terephthalate^[16] at the sun-facing front side of the device. However, optical simulations indicate that tandem

1. Introduction

Photovoltaic cells based on hybrid organic–inorganic lead halide perovskites have attracted significant interest from both

Dr. L. Gil-Escrig,^[†] M. Roß, A. Al-Ashouri, Prof. S. Albrecht
Young Investigator Group Perovskite Tandem Solar Cells
Helmholtz-Zentrum Berlin
Kekuléstraße 5, 12489 Berlin, Germany
E-mail: steve.albrecht@helmholtz-berlin.de

J. Sutter, Prof. C. Becker
Young Investigator Group Nano-SIPPE
Helmholtz-Zentrum Berlin
Albert-Einstein-Str. 16, 12489 Berlin, Germany

 The ORCID identification number(s) for the author(s) of this article can be found under <https://doi.org/10.1002/solr.202000553>.

^[†]Present address: Instituto de Ciencia Molecular, Universidad de Valencia, C/Catedrático J. Beltrán 2, Paterna, 46980 Valencia, Spain

© 2020 The Authors. Solar RRL published by Wiley-VCH GmbH. This is an open access article under the terms of the Creative Commons Attribution License, which permits use, distribution and reproduction in any medium, provided the original work is properly cited.

The copyright line for this article was changed on 17 December 2020 after original online publication.

DOI: 10.1002/solr.202000553

devices based on fully textured perovskite top cells conformally grown on silicon with random pyramidal microstructures,^[11,17–20] inverted pyramids,^[21] or sinusoidal structures^[22] would yield superior light trapping and reduced reflection and can thus enhance photocurrent generation in a broad spectral range.

When applying light trapping structures to perovskite/silicon tandem solar cells, a challenge that still remains is the way to fabricate conformal perovskite absorber layers on top of pyramidal microstructures, which are widely used for silicon solar cells and relevant on an industrial level. These textures are optimized including also the near infrared spectral range and have typical pyramid heights of several microns, thus being much larger than typical perovskite absorber layer thicknesses around 500 nm.

The aforementioned frequently used perovskite deposition methods relying on solution processing do not produce conformal layers and are therefore unsuitable to cover microscopically textured silicon substrates with pyramid size of up to 10 μm. To overcome this challenge, Sahli and coworkers used a hybrid process with conformal evaporation of the inorganic precursors and subsequently spin coating of the organic perovskite precursors, enabling yet the highest external quantum efficiencies reported to date for these tandem cells (compare also Figure S1, Supporting Information).^[23] However, the electric quality of the utilized perovskite absorber is limited in this approach as seen by the mediocre FF. Recently, mildly textured silicon was covered completely by a solution processed and very thick perovskite absorber films with very high perovskite/silicon tandem solar cell efficiency of up to 26%.^[9,24] However, here the texture had to be adapted toward smaller feature sizes with narrow height distributions to avoid shunting of the top cell.

Consequently, it is highly important to develop high-quality and conformal perovskite solar cells on typical pyramidal textures utilized for silicon to enable optimum light management and the integration toward standard silicon textures for in monolithic perovskite/silicon tandem solar cells.

An interesting alternative to solution-based or hybrid fabrication methods is the physical vapor deposition by coevaporation of precursors. Perovskite absorbers fabricated by coevaporation result in very smooth, highly conformal, and pinhole-free films allowing for excellent control over film thickness and composition.^[25–28] Moreover, the perovskite formation, composition, and its morphology can be influenced by the deposition rate of the precursors providing an additional parameter for optimization.^[29] To the best of our knowledge, so far, no reports on coevaporated perovskite solar cell devices fabricated on microscopically textured glass or silicon were reported, although there are numerous interesting reports on conformally evaporated bare films on these textures.^[2,28] As the preparation of complete perovskite/silicon tandem solar cells is very time and cost intensive, we decided to transfer the typical microscopic silicon textures onto glass substrates. This allows us to study and optimize the deposition of the perovskite on pyramidal microtextures in a simple and opaque device configuration. Furthermore, the perovskite PCE for this model system is, in contrast to tandem solar cells, directly and easily accessible.

In this work, fully vacuum-based perovskite solar cells are prepared on top of microscopically textured glass substrates with pyramid size of up to 9 μm. The microscopically textured glass resembles the typical pyramid topography of silicon solar cells as

a step toward monolithic tandem integration. We analyze the influence of the textures on the reflectance and external quantum efficiency (EQE). Moreover, we test three different methylammonium iodide (MAI) to lead iodide (PbI₂) rate ratios to improve the quality of the perovskite on the textured substrates. We show that optimized precursor ratios for textured substrates with higher PbI₂ rates enable a transient photoluminescence (TrPL) decay time above 0.75 μs, approaching that of planar substrates at around 1.2 μs. Finally, we show that using substrates textured with microscopic random pyramids of up to 9 μm height, a proof-of-concept efficiency of over 15% can be realized for textured perovskite single junctions that have a huge potential to improve the optics of fully textured monolithic perovskite/silicon tandems.

2. Results and Discussion

To fabricate the planar and microscopically textured substrates, 2.9 × 2.9 cm² Corning Eagle XG glasses were used as substrates for perovskite single junction solar cells. Both planar and textured samples were processed by imprint lithography as previously reported.^[30] As master for random pyramid textures, a 1–0–0 monocrystalline silicon wafer was etched in potassium hydroxide to generate pyramid heights of up to 9 μm. In addition, a polished silicon wafer was used as master for the planar references.

Figure 1 shows the imprint lithography process and the herein used planar as well as microtextured glass substrates device layouts. Figure 1a–c shows the imprint lithography process for textured and planar devices. Figure 1d shows the planar and textured solar cell device architecture together with the illumination direction and the pathways of the incoming light represented by yellow arrows. For more experimental details of the device fabrication, see Section “Device Fabrication.”

Figure 2a shows a 3D confocal microscopy image of textured glass substrates after the imprint lithography step. To analyze the height distribution of the random pyramid structures, the signal from the confocal microscope was filtered with a Gaussian filter and then further processed with a watershed algorithm to extract the location of local maxima and their grain boundaries (see Figure 2a). In addition, small grains were cut out to further reduce noise from the signal. The resulting height distribution of the random pyramid structure in the analyzed area *A* of 95.35 × 71.52 μm² is shown in Figure 2b. The root mean square height (*S_q*), which is calculated as $S_q = \sqrt{\frac{1}{A} \iint_A Z^2(x, y) dx dy}$, adds up to 1.1 μm, while the maximum and average pyramidal texture height *Z* in the analyzed area *A* is up to 9.1 μm and around 4.2 μm, respectively. The planar and textured imprinted substrates were sputtered conformally with indium tin oxide (ITO) to a layer thickness of at least 150 nm. Scanning electron microscopy (SEM) images of the sputtered ITO layer on the planar and textured substrates are shown in Figure 2c,d, respectively.

The textured substrates have a different topography and roughness compared with the untreated (planar) ones, such as commercial ITO or fluorine-doped tin oxide (FTO) that is typically utilized for perovskite single junctions,^[31,32] which can have an effect on the properties of the deposited perovskite film such as preferential orientation and the crystal grain size of the

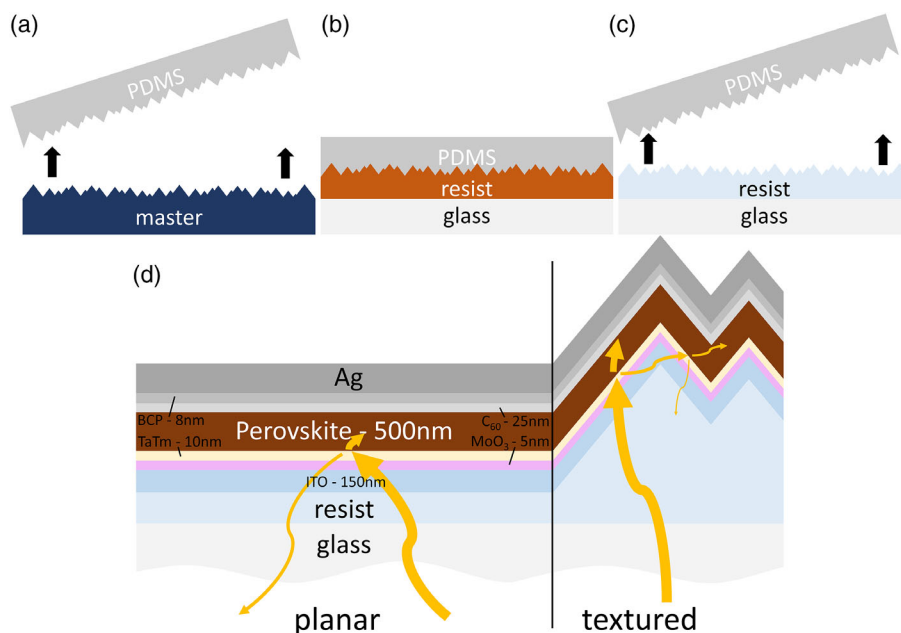


Figure 1. Imprint lithography process. a) The master structure is transferred inverse into a PDMS mold. b) Resist is spin-coated on glass substrate, imprinted, and cured by UV light. c) PDMS mold is lifted off to replicate the master structure on glass. d) Planar versus textured device architecture together with illumination direction.

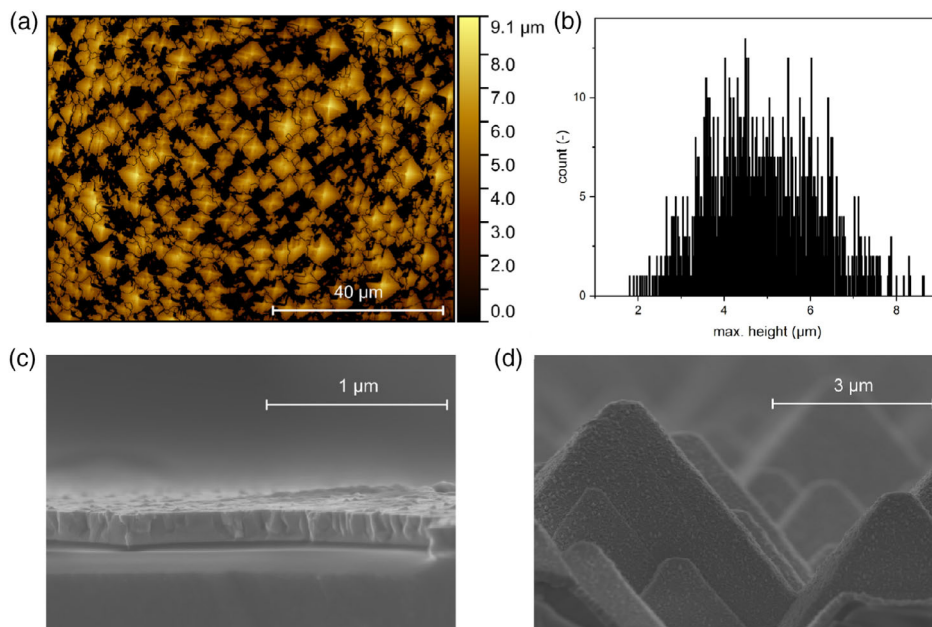


Figure 2. a) 3D confocal microscopy image of nanoimprint lithography textured glass substrate. b) Histogram of the pyramid height distribution. c,d) Scanning electron microscopy (SEM) images of planar and textured glass substrates with ITO layer, respectively.

perovskite.^[33] In view of this large difference in roughness between planar and textured substrates, three perovskite films using different MAI to PbI_2 ratios were evaporated on top of textured and planar substrates. For the preparation of the three different perovskite layers, the MAI deposition rate was kept constant at 1 \AA s^{-1} while varying the deposition rate of PbI_2 between 0.4 \AA s^{-1} (1:0.7), 0.6 \AA s^{-1} (1:1), and 0.9 \AA s^{-1} (1:1.5), referred to as perovskite films A, B, and C, respectively,

throughout this article. In a recent report it was shown that different ratios lead to a changing morphology and crystalline phase for the MAPbI_3 films.^[34,35] In addition, the different ratios can affect the growth of the perovskite and consequently the charge carrier transport, as it was published by Buonassisi et al.^[36]

X-ray diffraction (XRD) measurements were performed on the films to examine the formation of perovskite phases and

crystallinity (Figure S2, Supporting Information). In all evaporated films, the characteristic peaks of the perovskite were observed. All of them showed a diffraction peak at 2θ of 12.57° , indicating that there was a slight excess of unreacted PbI_2 in the films. This was more pronounced for the perovskite films B and C, prepared using a higher PbI_2 to MAI ratio. Hence, this demonstrates that this condition leads to an expected excess of crystalline PbI_2 . The transmittance of the evaporated perovskite films with different precursor ratios was also measured, showing the characteristic onset of high transmittance for the methylammonium lead iodide perovskite at 780 nm wavelength in all three different layers (Figure S3, Supporting Information). However, the optical transmission spectra of the perovskite films produced with PbI_2 excess showed a much lower transmittance, mainly in the visible and near-infrared range.

To study the detail on a nano- and micrometer level, cross-sectional SEM images were taken for all films. As intended, we indeed observe a substantial difference in the film morphology for the different component ratios used, as shown in

Figure 3a. The variation of the MAI: PbI_2 precursor ratio affects the perovskite morphology on both the planar and textured glass. On the planar glass, perovskite A (Figure 3a) showed rather large grains with a diameter about 600 nm. In contrast to this, the films B and C showed closely packed smaller grains with a diameter of about 50 nm. Figure 3a also shows that with the coevaporation process, it is possible to prepare conformal homogeneous perovskite layers on top of pyramidal textured glass which is in-line with recent reports.^[37] Moreover, the same trend on texture as for planar devices is observed, except for perovskite type A. In this case, the grains are formed like columns of 800 nm in size, with voids and defects in between. One possible explanation would be the different way of evaporation of the precursors used. It is known that the PbI_2 evaporates directly as a cone; meanwhile, the MAI has a very high vapor pressure and thus evaporates non-directional, as a cloud formation. Hence, the MAI is deposited in the same way independently of the substrate used (Figure S4, Supporting Information). Therefore, for film type A with a MAI/ PbI_2 ratio of 1:0.7, the film contains a

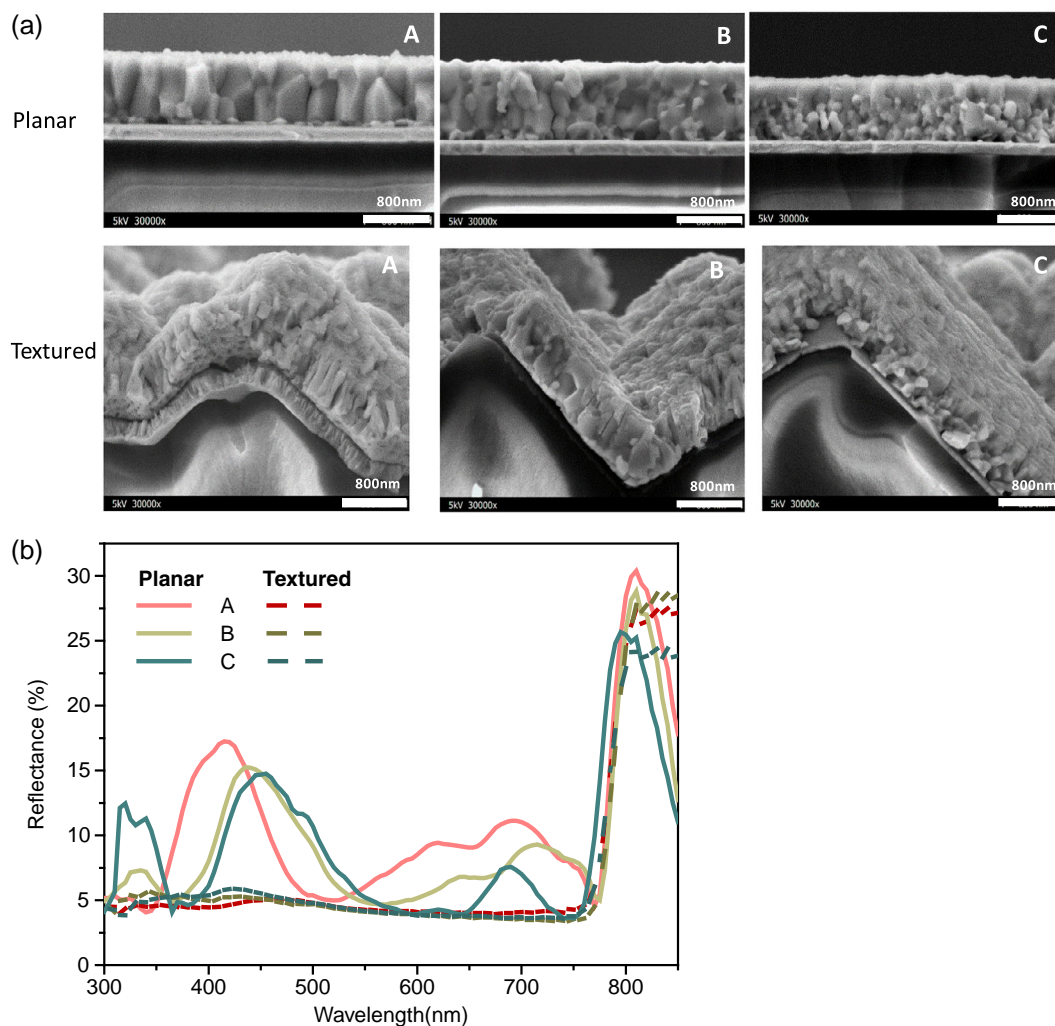


Figure 3. a) SEM cross-sectional images from full devices on planar and textured substrates with different precursor ratios. b) Reflectance spectra measured from the glass side for the three different precursor ratios: A (1:0.7), B (1:1), and C (1:1.5).

larger excess of MAI than when this perovskite film is deposited on the planar glass.

To measure the optical difference between the planar and the textured glasses, reflectance measurements were carried out for the three evaporated perovskite films (light incident on glass). Clearly, a reduction in the reflectance in the whole broadband wavelength range was observed when the film was evaporated on the textured substrate. This reduction is due to an increase of the in-coupling efficiency at the textured glass to ITO and the textured ITO to hole transport layer (HTL) and perovskite interfaces, allowing the device stack to strongly increase the overall absorption within the perovskite active layer. Looking at the different perovskite films A, B, and C, almost no difference was found for the three different perovskite films on the textured glass. However, the reflection spectrum changed when they were evaporated on the planar glass; the interference peak of maximum reflection shifted in wavelength from 410 to 430 to 460 nm for films A, B, and C, respectively, which we ascribe to differences in the film thickness ranging from 850 over 950 to 810 nm and potentially slight changes in the refractive index by the variation in the composition. In addition to that, on planar substrates the overall spectral reflectance between 500 and 750 nm wavelength was higher for film types A and B, using a lower PbI_2 rate during the deposition process.

To gain more knowledge on the perovskite quality and study the behavior of the charge carriers, we use TrPL on the different evaporated films on the HTL. The corresponding PL decays are found in **Figure 4**. A faster decay at early times was observed for all the samples measured, which is comparable to what has been reported so far.^[38] This initial decay might be attributed to charge transfer effects of, e.g., holes being transferred into the HTL.^[39] At later times, the transients decay monoexponentially, for which trap-assisted recombination in the bulk and at the HTL interface can be assigned as the underlying cause (the laser fluence of $\approx 30 \text{ nJ cm}^{-2}$ was set to match 1 sun equivalent charge generation). The extracted decay time from this part gives an estimate for the optoelectronic quality of the perovskite film/HTL stack. The decay times increase when going from film A, to B, to C, especially for the textured samples, with decay times increasing significantly from 170 ns (film A) to over 550 ns (film B), and finally to 750 ns (film C) for the highest PbI_2 amount. The increased PbI_2 rates transfer into different perovskite

composition as is also seen by the XRD patterns in Figure S2, Supporting Information. Thus, we can assume that an increased amount of PbI_2 improves the perovskite quality, either passivating the film surfaces or helping for a higher quality nucleation of the perovskite on textured substrates. This perovskite quality improvement was already observed in the SEM cross-sectional images (Figure 3) in which denser and similar sized grains were obtained for films B and C compared with the one with less PbI_2 content. Notably, the perovskite films on textured films show shorter decay times than on the planar films, which may be either related to higher nonradiative recombination in the perovskite film, or to an increased role of interface recombination due to the larger surface area on the textured substrates. For the highest PbI_2 ratio, the decay time on the textured substrate approaches the one of the planar substrates. This is in line with the aforementioned difference in the evaporation behavior of the two precursor materials. As PbI_2 shows a more direct evaporation behavior in contrast to the rather cloud-like behavior of the MAI, only the PbI_2 rate must be increased to compensate for the larger surface area.

Fully vacuum-processed perovskite solar cells using a p-i-n (so-called “inverted”) device layout were fabricated on top of planar and textured glass with the different precursor rates as presented earlier. Molybdenum oxide (MoO_3 , 5 nm) and TaTm (10 nm) were used as HTL, then a 500 nm-thick perovskite film was evaporated, and C_{60} (25 nm) and bathocuproine (BCP) (8 nm) were used as electron transport layers (ETLs). Finally, 100 nm of silver electrode was evaporated to complete the devices. The HTL, MAPbI_3 , and ETL thicknesses were adapted for the textured devices to compensate the larger surface area. Hence, all the standard thicknesses mentioned before are multiplied by a factor of 1.8. **Figure 5** shows the current–voltage (J – V) data under illumination and in dark for the different substrates and precursor ratios.

First, for the three planar solar cells the photovoltaic performance was evaluated. Figure 5a shows the J – V characteristics under simulated 1 sun equivalent illumination of the best solar cells obtained and, in the inset, the maximum power point (MPP) tracking measured over a period of 12 h. Their photovoltaic parameters are shown in **Table 1** and a statistical comparison is reported from over 50 individual solar cell devices being processed for this comparison in **Table 1** and **Figure S5**, Supporting

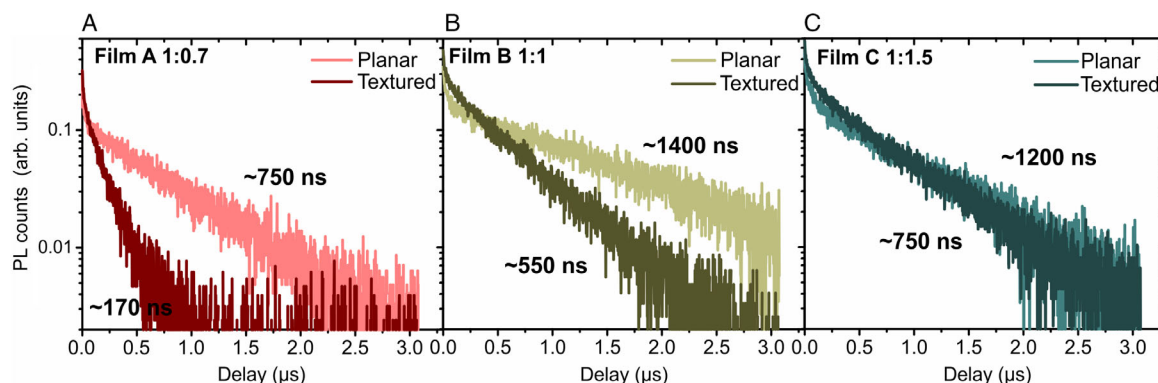


Figure 4. Transient photoluminescence (TrPL) decay of perovskite films A, B, and C deposited on the hole transporting layer TaTm using planar (lighter colors) and textured substrates (darker colors).

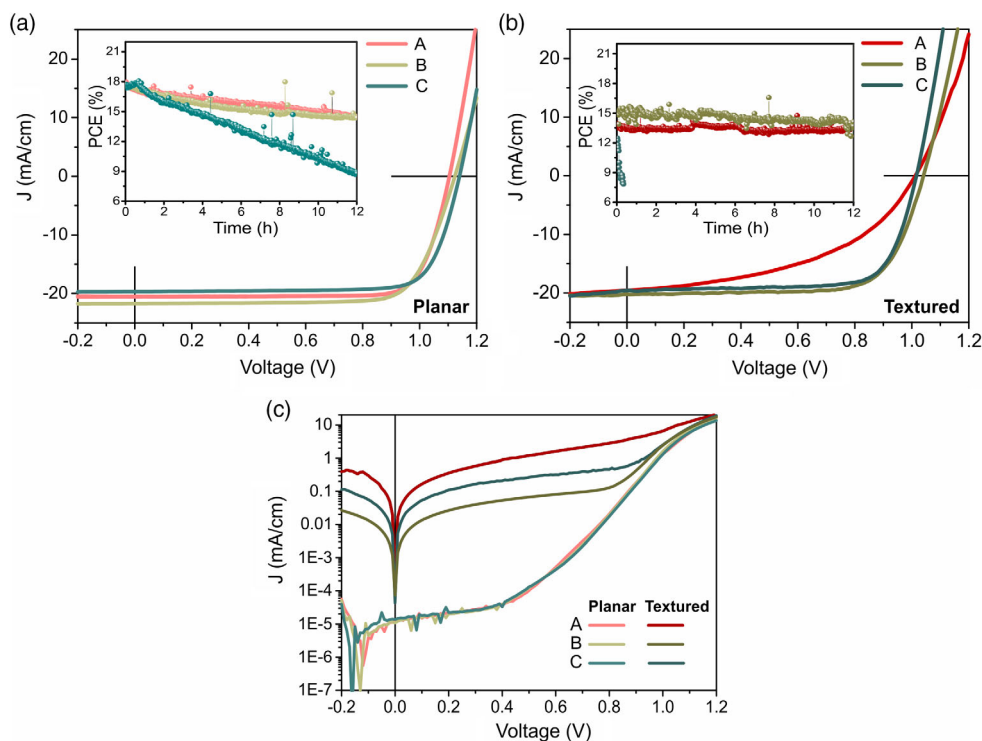


Figure 5. Current–density–voltage (J – V) curves under 100 mW cm^{-2} illumination of the a) planar and b) textured device architectures using film types A, B, and C. The inset shows respective MPP tracking over a period of 12 h. c) The corresponding J – V curves measured in dark conditions.

Table 1. Photovoltaic parameters from J – V scans under illumination for the best perovskite solar cells with different perovskite film types A, B, and C, for planar and textured glass. The standard deviation based on over 50 individual devices that were fabricated for this comparison is included as well..

	J_{sc} [mA cm^{-2}]	J_{sc} from EQE [mA cm^{-2}]	V_{oc} [V]	FF [%]	PCE [%]
Flat A	20.48 ± 0.6	20.89 ± 0.5	1.10 ± 0.01	80 ± 0.6	18.02 ± 0.6
Flat B	20.86 ± 0.3	21.04 ± 0.3	1.12 ± 0.01	78 ± 1.1	18.22 ± 0.3
Flat C	19.28 ± 0.1	20.76 ± 0.1	1.14 ± 0.01	76 ± 0.5	16.70 ± 0.2
Textured A	19.55 ± 1.1	20.38 ± 1.0	1.012 ± 0.1	47 ± 5.2	9.99 ± 1.5
Textured B	20.23 ± 0.1	21.03 ± 0.2	1.041 ± 0.01	73 ± 2.3	15.37 ± 0.6
Textured C	19.58 ± 0.5	21.08 ± 0.6	1.061 ± 0.02	74 ± 6.3	14.72 ± 1.6

Information. The reference devices on planar substrate yield efficiencies up to 18.22% which is comparable to commercial substrates using the same HTLs.^[40] Looking at the performance, we find an increase mainly in V_{oc} (devices type B and C), which is in line with the aforementioned TrPL analysis, showing a higher TrPL lifetime for films B and C. A higher TrPL lifetime can be correlated to a higher perovskite bulk and/or interface quality, which, in turn, expresses in a larger PL quantum yield and thus larger potential for higher V_{oc} .^[41] However, the overall PCE was lower for device type C, due to lower J_{sc} and FF. Moreover, a faster decay in the efficiency was observed when the PCE was

recorded for 12 h under 1 sun illumination. For the devices with the other two ratios (A and B), the PCE and stability were comparable and in line with existing results on planar devices in which they used the same p–i–n configuration,^[42] showing around 20% loss in efficiency after 12 h continuous MPP tracking. However, statistically (Figure S5, Supporting Information), for the solar cells type A, a larger spread of the values was noted. We noted that all devices showed a rather low and comparable dark leakage current, indicating a good diode behavior (Figure 5c). The textured devices, on the contrary, show more spread in the sample variation and higher dark leakage currents potentially resulting from local thickness variations of the absorber layer on top of the textured substrates leading to partial shunting. Interestingly, the relative stability (see Figure S6, Supporting Information) for textured devices A and B with less than 10% efficiency loss (relative) is higher than for planar cells being subject of further investigations.

Then, the different perovskites were tested on top of the textured glass. Figure 5b shows the J – V curves under illumination and the long period MPP tracking to assess stability. The most striking difference comes with the devices with lower content of PbI_2 (device type A). The less-ordered morphology observed in this perovskite films (Figure 3 IV) together with the short TrPL lifetime, shown in Figure 4, is associated with the low V_{oc} and FF. Interestingly, despite the lower performance, the stability of device A was comparable or even better than the solar cells with films type B and C. Similar efficiencies were found for the perovskite devices with more content of PbI_2 (types B and C);

however, the device type B presented a higher stability, higher V_{oc} , and in the end better efficiencies, rendering the 1:1 ratio to be a good compromise between stability and efficiency.

Fabricating conformal and efficient perovskite solar cells on top of pyramidal structures has been a challenge so far. Hence, the yield has been much higher for the planar than for the textured solar cells, with 90% and 60% of the devices working, respectively. One possible explanation for the slightly lower performance of the average (see Figure S5, Supporting Information for more statistics) and best textured versus planar samples could be the larger interface area to the electron selective C_{60} contact. It has previously been shown that this contact is strongly limiting due to the higher nonradiative losses at this interface.^[43] We thus speculate that the V_{oc} decrease is more severe with an increase in the limiting interface area. In addition, the large dark current for textured devices (Figure 5c) can be a potential reason for the reduction in FF and V_{oc} . However, the efficiencies presented in this work are, to the best of our knowledge, the first reported until now for conformal and pyramidal microtextured glass substrates enabling fully evaporated perovskite solar cells and show the proof-of-concept for coevaporation on typically textured silicon substrates.

The EQE was measured to quantify if the reduction in reflection can translate into higher photocurrent generation in the solar cell device. In Figure 6, the EQE and the (1-reflectance, 1-R) are shown for the precursor ratio resulting in film B for planar and textured device architectures. In the range between 300 and 400 nm, the EQE of the textured sample is lower potentially due to parasitic absorption losses in the functional layers at the front side. Between 400 and 500 nm however, the strong reduction in reflection is translated into a higher EQE in this regime. Between 550 and 750 nm the reduced reflection for textured devices does not yield higher EQEs. It remains open whether this is due to the fact that longer wavelength light is absorbed closer to the C_{60} interface, which might limit charge collection efficiency, or due to a lower optoelectronic absorber quality lowering the overall charge collection at short circuit. We note that the true

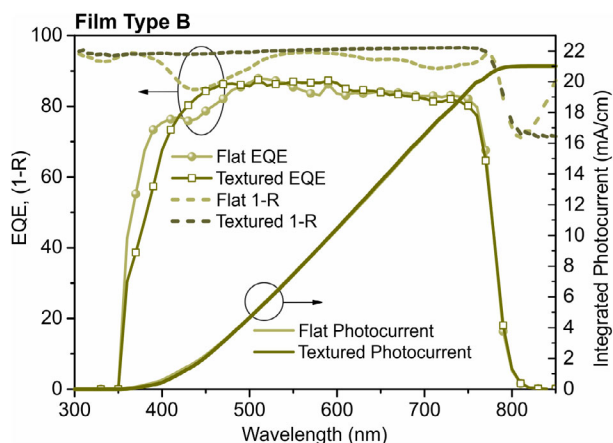


Figure 6. External quantum efficiency (EQE) and reflection spectra (depicted as 1-reflection) on the left y-axis together with the integrated photocurrent from EQE spectra for solar cells with perovskite film type B on planar and textured glass.

optical benefit with the potential to gain $>1 \text{ mA cm}^{-2}$ photocurrent^[11,17,19] from the microscopic textures will be gained in the monolithic tandem solar cell (see Figure S1, Supporting Information). Overall the partial increase and decrease in the EQE spectra result in very similar integrated J_{sc} between planar and textured devices. Figure S7, Supporting Information shows the EQE and the (1-reflectance) for the other two perovskites (A and C). A slightly red-shifted EQE onset from the textured devices was observed in the perovskite type C which is in line with the moderate improvement in the J_{sc} compared with the planar devices. Thus, although the EQE spectra do not evidence a huge improvement in collected photocurrent, the light in-coupling is indeed improved as shown by the reflection and expected red-shift of electroluminescence (EL), mainly in perovskite type C (Figure S8, Supporting Information).^[44] In this particular case, the blue shift of the EL peak for the solar cells type C is due to a change in the optical bandgap, which is appreciable in the transmittance spectra (Figure S2, Supporting Information) and also in the absolute PL (see Figure S9, Supporting Information). The increase in the PbI_2 content leads to an increase in about 10 mV in the optical bandgap for sample C with a slightly higher increase for the planar devices. Furthermore, with the stability measurements shown earlier (Figure 5), we can state that solar cells with these perovskite films degrade faster than the others under illumination, although giving the highest PL lifetime at least for the textured devices. That lead iodide excess can lead to reduced long-term stability has already been observed for solution-based perovskites^[45] and is currently subject of scientific discussion.^[46] Interestingly, the absorption onset remains the same between planar and textured seen in EQE, which shows that light trapping within the absorber layer for perovskite films is not dominant here.^[44]

3. Conclusion

So far, no reports on coevaporated perovskite solar cell devices fabricated on pyramidal microtextured substrates were published. Efficiencies above 15% were reached in this work for fully evaporated and microscopically textured perovskite solar cells. Perovskite single junction solar cells were built on microscopically textured and planar glass substrates, prepared by imprint lithography. Conformal perovskite layers were coevaporated on top of planar and pyramidal textured glass to analyze the film formation process in a model system applicable to textured silicon and to improve the light management in the perovskite devices. A clear reduction in reflectance losses with the textured substrates was observed yielding a partially enhancement of the EQE with texture. Moreover, with the MAI to PbI_2 precursor ratio adjustment, the perovskite's quality was improved on the textured substrate, and different rate behavior for volatile MAI versus PbI_2 was found. Optimized precursor ratios for textured substrates enabled a TrPL decay time approaching that of planar substrates. With the findings on the evaporation behavior as function of surface area, the lack of reports about textured coevaporated tandems might be solved by optimizing the growth of the perovskite for this type of substrates.

4. Experimental Section

Fabrication of Planar and Pyramidally Textured Substrates: Corning Eagle XG glasses ($5.8 \times 5.8 \text{ cm}^2$) with a thickness of 1.1 mm were used as glass substrates. Both planar and textured samples were processed by imprint lithography. For the imprinting process, 0.7 mL of two components UV light curable resist OrmoComp was spin-coated 30 s at 3000 rpm on the glass substrates, prebaked at 80°C , imprinted with the structured molds, and cured 5 min with a broadband UV source. Two-component PDMS Elastosil was poured on the master structures, cured 3 h at 50°C , and accordingly peeled off as imprint lithography mold with inverse master structure. To increase transparency of the resist layers, they were further annealed for 3 h at 150°C . Textured and planar imprinted glass substrates were then cut into $2.9 \times 2.9 \text{ cm}^2$ pieces. A ceramic ITO target, with a power of 70 W, and a 0.2% oxygen/argon sputter gas mixture were utilized for all depositions. In a posttreatment step, ITO was annealed in ambient air for 10 min at 200°C .

Vacuum Deposition: The vacuum chamber was equipped with six temperature-controlled evaporation sources (CreaPhys) fitted with ceramic crucibles. The sources were directed upward with an angle of $\approx 90^\circ$ with respect to the bottom of the evaporator. The substrate holder to evaporation sources distance was $\approx 20 \text{ cm}$. Three quartz crystal microbalance (QCM) sensors were used, two for monitoring the deposition rate of each evaporation source and the third one close to the substrate holder monitoring the total deposition rate. For thickness calibration, the charge transport materials were individually sublimed. A calibration factor was obtained by comparing the thickness inferred from the QCM sensors with that measured with a mechanical profilometer (Ambios XP1). Then, the materials were sublimed at temperatures ranging from 160°C to $>300^\circ\text{C}$, and the evaporation rate was controlled by separate QCM sensors obtaining precisely the deposited thickness.

Device Fabrication: To fabricate the solar cells, textured and planar imprinted glass substrates were cleaned and transferred to the vacuum chamber, as explained in the Supporting Information. This vacuum chamber was used to sublime the $\text{N}_4, \text{N}_4, \text{N}_4'', \text{N}_4'''$ -tetra([1,1'-biphenyl]-4-yl)-[1,1':4,1''-terphenyl]-4,4''-diamine (TaTm), C_{60} , and BCP together with PbI_2 and MAI. As it is not easy to determine the average height or volume of a pure MAI film, the calibration of the QCM sensors is not straightforward. In addition, the adsorption rate of MAI is different in the presence of evaporating PbI_2 in the chamber. As a result, the QCM readings are correlated with off-line analysis such X-ray of the prepared films.^[47] For the preparation of the three different perovskite layers, the MAI deposition rate was kept constant at 1 \AA s^{-1} while varying the deposition rate of PbI_2 between 0.4 \AA s^{-1} (1:0.7), 0.6 \AA s^{-1} (1:1), and 0.9 \AA s^{-1} (1:1.5), referred to as perovskite films A, B, and C, respectively, throughout this article. The source temperature of the MAI was kept at 70°C and the PbI_2 varied between 250 and 305°C . The deposition rate for the TaTm and C_{60} was 0.5 and 0.3 \AA s^{-1} for the thinner BCP layer. MoO_3 and Ag were evaporated in a third vacuum chamber using tantalum boats by applying currents ranging from 2 to 5 A.

Device Characterization: SEM images in top and cross-sectional view were performed on a Hitachi S-4800 microscope operating at an accelerating voltage of 2 kV over platinum-metallized samples.

Absorption and reflectance spectra were collected using fiber optics-based Avantes Avaspec2048 Spectrometer. Reflectance and transmittance spectra were measured from 300 to 850 nm with a step size of 5 nm using a PerkinElmer Lambda 1050 UV/vis/NIR double beam spectrophotometer. For reflectance measurements, an integrating sphere was used.

X-ray diffractograms were collected with Panalytical Empyrean diffractometer equipped with a Cu anode operated at 45 kV and 40 mA and a PIXcel 1D detector in scanning line mode. Single scans were acquired in the $2\theta = 5^\circ$ – 50° range, in Bragg–Bretano geometry in air.

The J – V curves for the solar cells were recorded using Keithley 2612A source meter in a -0.2 and 1.2 V range, with 0.01 V steps and integrating signal for 20 ms after 10 ms delay, corresponding to a speed of about 0.3 V s^{-1} . The devices were illuminated under a Wavelabs Sinus 70 LED solar simulator. The light intensity was calibrated before every measurement using a calibrated Si reference solar cell stability measurements,

which were recorded using a MPP tracker system, with a white LED light source under 1 sun equivalent, developed by Candlelight. During the stability measurements, solar cells were kept in N₂; temperature was kept at 300 K using a water-circulating cooling system. The EQE was estimated using the cell response at different wavelength (measured with a white light halogen lamp in combination with band-pass filters), where the solar spectrum mismatch was corrected with a calibrated silicon reference cell (MiniSun simulator by ECN, from the Netherlands).

TrPL measurements were carried out in a home-built setup (Unold laboratory of HZB, Wannsee) using 660 nm excitation laser light from a supercontinuum light source (SuperK) with a 25 – $35 \text{ }\mu\text{m}$ spot size. The whole PL emission was collected through a photomultiplier and a time-correlated single photon counting technique. The fluence was set to $\approx 20 \text{ nJ cm}^{-2}$ to resemble close to 1 sun equivalent excited charge carrier density. For confocal microscopy, a KEYENCE laser scanning confocal microscope was used. Images were taken with $150\times$ magnification. Further image processing was carried out with the software Gwyddion.

Supporting Information

Supporting Information is available from the Wiley Online Library or from the author.

Acknowledgements

The authors thank David Eisenhauer from HZB for support in glass texturing by nanoimprint lithography. They also thank Thomas Unold from HZB, Department of Structure and Dynamics of Energy Materials and his team for providing the transient PL setup infrastructure and data analysis routines. The authors thank the technicians and engineers T. Luřky, H. Heinz, M. Gabernig, C. Klimm, C. Ferber, M. Muske (Institute for Silicon Photovoltaics), and Tobias Henschel (PVcomB) for technical assistance. For XRD measurements, the X-Ray CoreLab, K. A. Mazzio, and R. Gunder are acknowledged. The authors acknowledge funding from the Federal Ministry of Education and Research (BMBF) for funding of the Young Investigator Group Perovskite Tandem Solar Cells within the program "Materialforschung für die Energiewende" (grant no. 03SF0540), as well as for the SNaPSHoTs Project (grant no. 01IO1806). In addition, the authors acknowledge funding from the Helmholtz Association within the HySPRINT Innovation lab project, and the HyPerCells Joint 728 Graduate School. Open access funding enabled and organized by Projekt DEAL.

Conflict of Interest

The authors declare no conflict of interest.

Keywords

coevaporation, perovskite, tandem solar cells, vacuum-processed solar cells

Received: September 7, 2020

Revised: October 22, 2020

Published online: November 17, 2020

[1] W. Li, Z. Wang, F. Deschler, S. Gao, R. H. Friend, A. K. Cheetham, *Nat. Rev. Mater.* **2017**, *2*, 16099.

[2] J. Huang, Y. Yuan, Y. Shao, Y. Yan, *Nat. Rev. Mater.* **2017**, *2*, 17042.

[3] T. M. Brenner, D. A. Egger, L. Kronik, G. Hodes, D. Cahen, *Nat. Rev. Mater.* **2016**, *1*, 15007.

- [4] M. A. Green, E. D. Dunlop, D. H. Levi, J. Hohl-Ebinger, M. Yoshita, A. W. Y. Ho-Baillie, *Prog. Photovoltaics Res. Appl.* **2019**, *27*, 565.
- [5] M. Jošt, L. Kegelmann, L. Korte, S. Albrecht, *Adv. Energy Mater.* **2020**, *10*, 1904102.
- [6] J.-F. Guillemoles, T. Kirchartz, D. Cahen, U. Rau, *Nat. Photonics* **2019**, *13*, 501.
- [7] J. Burschka, N. Pellet, S.-J. Moon, R. Humphry-Baker, P. Gao, M. K. Nazeeruddin, M. Grätzel, *Nature* **2013**, *499*, 316.
- [8] D. Wang, J. Zheng, X. Wang, J. Gao, W. Kong, C. Cheng, B. Xu, *J. Energy Chem.* **2019**, *38*, 207.
- [9] B. Chen, Z. J. Yu, S. Manzoor, S. Wang, W. Weigand, Z. Yu, G. Yang, Z. Ni, X. Dai, Z. C. Holman, J. Huang, *Joule* **2020**, *4*, 850.
- [10] A. Al-Ashouri, A. Magomedov, M. Roß, M. Jošt, M. Talaikis, G. Chistiakova, T. Bertram, J. A. Márquez, E. Köhnen, E. Kasparavičius, S. Levenco, L. Gil-Escrig, C. J. Hages, R. Schlatmann, B. Rech, T. Malinauskas, T. Unold, C. A. Kaufmann, L. Korte, G. Niaura, V. Getautis, S. Albrecht, *Energy Environ. Sci.* **2019**, *12*, 3356.
- [11] R. Santbergen, R. Mishima, T. Meguro, M. Hino, H. Uzu, J. Blanker, K. Yamamoto, M. Zeman, *Opt. Express* **2016**, *24*, A1288.
- [12] D. T. Grant, K. R. Catchpole, K. J. Weber, T. P. White, *Opt. Express* **2016**, *24*, A1454.
- [13] L. Mazzarella, Y.-H. Lin, S. Kirner, A. B. Morales-Vilches, L. Korte, S. Albrecht, E. Crossland, B. Stannowski, C. Case, H. J. Snaith, R. Schlatmann, *Adv. Energy Mater.* **2019**, *9*, 1803241.
- [14] M. Jošt, S. Albrecht, L. Kegelmann, C. M. Wolff, F. Lang, B. Lipovšek, J. Krč, L. Korte, D. Neher, B. Rech, M. Topič, *ACS Photonics* **2017**, *4*, 1232.
- [15] S. Manzoor, Z. J. Yu, A. Ali, W. Ali, K. A. Bush, A. F. Palmstrom, S. F. Bent, M. D. McGehee, Z. C. Holman, *Sol. Energy Mater. Sol. Cells* **2017**, *173*, 59.
- [16] M. Jaysankar, M. Filipič, B. Zielinski, R. Schmagel, W. Song, W. Qiu, U. W. Paetzold, T. Aernouts, M. Debucquoy, R. Gehlhaar, J. Poortmans, *Energy Environ. Sci.* **2018**, *11*, 1489.
- [17] D. A. Jacobs, M. Langenhorst, F. Sahli, B. S. Richards, T. P. White, C. Ballif, K. R. Catchpole, U. W. Paetzold, *J. Phys. Chem. Lett.* **2019**, *10*, 3159.
- [18] M. Jošt, E. Köhnen, A. B. Morales-Vilches, B. Lipovšek, K. Jäger, B. Macco, A. Al-Ashouri, J. Krč, L. Korte, B. Rech, R. Schlatmann, M. Topič, B. Stannowski, S. Albrecht, *Energy Environ. Sci.* **2018**, *11*, 3511.
- [19] L. Mazzarella, M. Werth, K. Jäger, M. Jošt, L. Korte, S. Albrecht, R. Schlatmann, B. Stannowski, *Opt. Express* **2018**, *26*, A487.
- [20] F. E. Subhan, A. D. Khan, A. D. Khan, N. Ullah, M. Imran, M. Noman, *RSC Adv.* **2020**, *10*, 26631.
- [21] B. Schneider, N. Lal, S. Baker-Finch, T. White, *Opt. Express* **2014**, *22*, A1422.
- [22] D. Chen, P. Manley, P. Tockhorn, D. Eisenhauer, G. Köppel, M. Hammerschmidt, S. Burger, S. Albrecht, C. Becker, K. Jäger, *J. Photonics Energy* **2018**, *8*, 022601.
- [23] F. Sahli, J. Werner, B. A. Kamino, M. Bräuninger, R. Monnard, B. Paviet-Salomon, L. Barraud, L. Ding, J. J. Diaz Leon, D. Sacchetto, G. Cattaneo, M. Despeisse, M. Boccard, S. Nicolay, Q. Jeangros, B. Niesen, C. Ballif, *Nat. Mater.* **2018**, *17*, 820.
- [24] Y. Hou, E. Aydin, M. De Bastiani, C. Xiao, F. H. Isikgor, D.-J. Xue, B. Chen, H. Chen, B. Bahrami, A. H. Chowdhury, A. Johnston, S.-W. Baek, Z. Huang, M. Wei, Y. Dong, J. Troughton, R. Jalmood, A. J. Mirabelli, T. G. Allen, E. Van Kerschaver, M. I. Saidaminov, D. Baran, Q. Qiao, K. Zhu, S. De Wolf, E. H. Sargent, *Science* **2020**, *367*, 1135.
- [25] M. Liu, M. B. Johnston, H. J. Snaith, *Nature* **2013**, *501*, 395.
- [26] J. Borchert, R. L. Milot, J. B. Patel, C. L. Davies, A. D. Wright, L. Martínez Maestro, H. J. Snaith, L. M. Herz, M. B. Johnston, *ACS Energy Lett.* **2017**, *2*, 2799.
- [27] E. Erdenebileg, L. E. Scholz, A. Hofacker, C. Koerner, K. Leo, *Energy Technol.* **2017**, *5*, 1606.
- [28] L. Cojocar, K. Wienands, T. W. Kim, S. Uchida, A. J. Bett, S. Rafizadeh, J. C. Goldschmidt, S. W. Glunz, *ACS Appl. Mater. Interfaces* **2018**, *10*, 26293.
- [29] B. Dänekamp, N. Droseros, F. Palazon, M. Sessolo, N. Banerji, H. J. Bolink, *ACS Appl. Mater. Interfaces* **2018**, *10*, 36187.
- [30] D. Eisenhauer, C. T. Trinh, D. Amkreutz, C. Becker, *Sol. Energy Mater. Sol. Cells* **2019**, *200*, 109928.
- [31] W. Nie, H. Tsai, R. Asadpour, J. C. Blancon, A. J. Neukirch, G. Gupta, J. J. Crochet, M. Chhowalla, S. Tretiak, M. A. Alam, H. L. Wang, A. D. Mohite, *Science* **2015**, *347*, 522.
- [32] H. Zhou, Q. Chen, G. Li, S. Luo, T. B. Song, H. S. Duan, Z. Hong, J. You, Y. Liu, Y. Yang, *Science* **2014**, *345*, 542.
- [33] E. Climent-Pascual, B. C. Hames, J. S. Moreno-Ramírez, A. L. Álvarez, E. J. Juárez-Pérez, E. Mas-Marza, I. Mora-Seró, A. de Andrés, C. Coya, *J. Mater. Chem. A* **2016**, *4*, 18153.
- [34] F. Palazon, D. Pérez-del-Rey, B. Dänekamp, C. Dreessen, M. Sessolo, P. P. Boix, H. J. Bolink, *Adv. Mater.* **2019**, *31*, 1902692.
- [35] B. Dänekamp, C. Müller, M. Sendner, P. P. Boix, M. Sessolo, R. Lovrincic, H. J. Bolink, *J. Phys. Chem. Lett.* **2018**, *9*, 2770.
- [36] S. Wiegold, J.-P. Correa-Baena, L. Nienhaus, S. Sun, K. E. Shulenberger, Z. Liu, J. S. Tresback, S. S. Shin, M. G. Bawendi, T. Buonassisi, *ACS Appl. Energy Mater.* **2018**, *1*, 6801.
- [37] T. Abzieher, J. A. Schwenzler, S. Moghadamzadeh, F. Sutterlüti, I. M. Hossain, M. Pfau, E. Lotter, M. Hetterich, B. S. Richards, U. Lemmer, M. Powalla, U. W. Paetzold, *IEEE J. Photovoltaics* **2019**, *9*, 1249.
- [38] V. S. Chirvony, K. S. Sekerbayev, D. Pérez-del-Rey, J. P. Martínez-Pastor, F. Palazon, P. P. Boix, T. I. Taurbayev, M. Sessolo, H. J. Bolink, *J. Phys. Chem. Lett.* **2019**, *10*, 5167.
- [39] B. Krogmeier, F. Staub, D. Grabowski, U. Rau, T. Kirchartz, *Sustain. Energy Fuels* **2018**, *2*, 1027.
- [40] A. Babaei, K. P. S. Zanoni, L. Gil-Escrig, D. Pérez-del-Rey, P. P. Boix, M. Sessolo, H. J. Bolink, *Front. Chem.* **2020**, *7*, 936.
- [41] T. Kirchartz, J. A. Márquez, M. Stolterfoht, T. Unold, *Adv. Energy Mater.* **2020**, *10*, 1904134.
- [42] A. Babaei, C. Dreessen, M. Sessolo, H. J. Bolink, *RSC Adv.* **2020**, *10*, 6640.
- [43] M. Stolterfoht, P. Caprioglio, C. M. Wolff, J. A. Márquez, J. Nordmann, S. Zhang, D. Rothhardt, U. Hörmann, Y. Amir, A. Redinger, L. Kegelmann, F. Zu, S. Albrecht, N. Koch, T. Kirchartz, M. Saliba, T. Unold, D. Neher, *Energy Environ. Sci.* **2019**, *12*, 2778.
- [44] F. Staub, T. Kirchartz, K. Bittkau, U. Rau, *J. Phys. Chem. Lett.* **2017**, *8*, 5084.
- [45] F. Liu, Q. Dong, M. K. Wong, A. B. Djurišić, A. Ng, Z. Ren, Q. Shen, C. Surya, W. K. Chan, J. Wang, A. M. C. Ng, C. Liao, H. Li, K. Shih, C. Wei, H. Su, J. Dai, *Adv. Energy Mater.* **2016**, *6*, 1502206.
- [46] B. Roose, K. Dey, Y.-H. Chiang, R. H. Friend, S. D. Stranks, *J. Phys. Chem. Lett.* **2020**, *11*, 6505.
- [47] O. Malinkiewicz, A. Yella, Y. H. Lee, G. M. Espallargas, M. Graetzel, M. K. Nazeeruddin, H. J. Bolink, *Nat. Photonics* **2014**, *8*, 128.